Electro-Thermal and -Mechanical Model of Thermal Breakdown in Multilayered Dielectric Elastomers

Line Riis Christensen, Ole Hassager, and Anne Ladegaard Skov

Danish Polymer Centre, Department of Chemical and Biochemical Engineering,

Technical University of Denmark, 2800 Lyngby, Denmark

Abstract

Multiple breakdown phenomena may take place when operating dielectric elastomers. Thermal breakdown, which occurs due to Joule heating, becomes of special importance when using multilayered stacks of dielectric elastomers, due to the large volume-to-surface-area-ratio. In this article, a 2D axisymmetric finite-element model of a multilayered stack of dielectric elastomers is set up in COMSOL Multiphysics®. Both the electro-thermal and electro-mechanical couplings are considered, allowing for determination of the onset of thermal breakdown. Simulation results show that an entrapped particle in the dielectric elastomer drastically reduces the possible number of layers in the stack. Furthermore, the possible number of layers is greatly affected by the ambient temperature and the applied voltage. The performance of three hyperelastic material models for modelling the elastomer deformation are compared, and it is established that the Gent model yields the most restrictive prediction of breakdown point, while the Ogden model yields the least restrictive estimation.

Topical Headings: Transport Phenomena and Fluid Dynamics

Keyword: Dielectric elastomer, Thermal breakdown, Electro-thermal and -mechanical model, Multilayered dielectric elastomers, Hyperelastic material model.

Introduction

In recent decades, interest in and research into dielectric elastomers (DEs) have increased dramatically, due to the possibilities of an electromechanical transducer being used both

as an actuator, a sensor, and a generator[1–3]. DEs can be used for a wide range of applications, such as artificial muscles[4–7], wave energy harvesters[8,9], and Braille displays[10,11].

A DE is composed of an elastomer layer sandwiched between two compliant electrodes, and upon applying an external voltage to the electrodes, electrostatic forces are generated between the electrode layers. The electrostatic pressure on the flexible elastomer film causes it to reduce in thickness while increasing in area, in order to retain a constant volume due to it being incompressible. In this manner, electrical energy is converted into mechanical energy. The driving force for the actuation mechanism is reduced charge density upon an increase in electrode area[1,2,12]. When the applied voltage is turned off, the elastomer regains its original shape. An illustration of a DE and its working principle is presented in Figure 1.

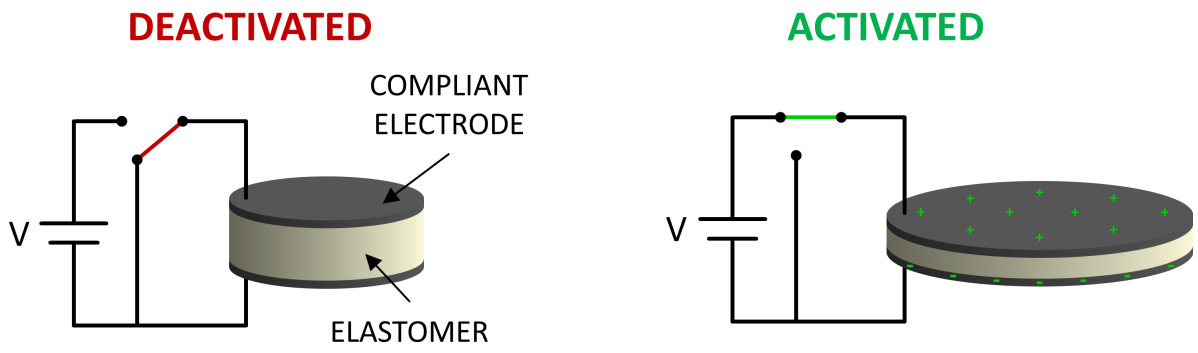

Figure 1: Working principle of a dielectric elastomer. The incompressible elastomer layer reduces in thickness while increasing in area when an external voltage is applied to the electrode layers.

Several elastomer materials are commonly used for the elastomer layer, including acrylic, polyurethane, natural rubber, and silicone[3,12], the latter of which is most popular, due to its high efficiency, reliability and fast response times[12]. With respect to electrode layers, the two commonest types of materials used in this regard are carbon grease and thin metal films such as gold or silver[13].

DEs can be configured in many ways, depending on the desired application, mechanical deformation, and operating strain[14]. Extender, unimorph, bimorph, diaphragm and tube configurations are examples of some of the configurations commonly seen in products[10,15]. When operating DEs in acutator mode, the achievable mechanical force can be increased by stacking DEs on top of each other, such that the electrode and elastomer

layers alternate[13,16]. When operating DEs in generator mode, the amount of harvested energy can also be optimised by employing a stacked configuration of DEs[17].

Several types of electrical ageing may occur when DEs are operated, and these can be subdivided into two main categories: Degradation mechanisms and breakdown mechanisms[18,19]. The slow degradation mechanisms lead to electrical trees and water trees[20,21], and they take more than 15 minutes from initiation to full material breakdown. On the contrary, breakdown mechanisms are somewhat instantaneous and include partial discharge[22], electromechanical breakdown[23], electrical breakdown[24,25], and thermal breakdown[26–28]. Figure 2 gives an overview of the different electrical ageing mechanisms that may occur in DEs as a function of electric field and time.

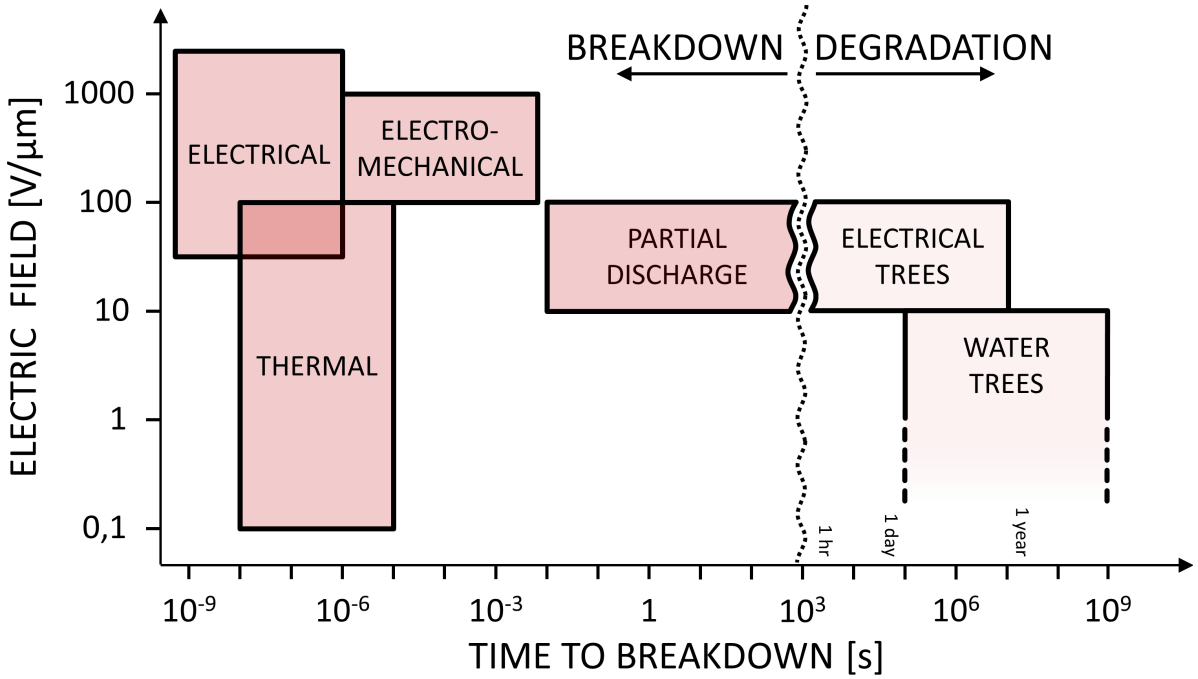

Figure 2: Types of electrical ageing that may occur in dielectric elastomers.

When seeking to improve the performance, stability, and lifetime of DEs, it is essential to take into account these different ageing mechanisms. Several studies have examined the combined effect of electrical and mechanical forces, in order to gain a broader understanding of electrical[23,29–32] and electromechanical[30–37] breakdowns in DEs. These studies involve both experimental testing as well as mathematical modelling of the system.

However, to the best of our knowledge, the number of studies looking into thermal breakdown in DEs is very limited. Previously, we set up a finite-element electro-thermal

(ET) model to examine the effect of Joule heating in multilayered DEs[38]. A simplified analytical model was set up and solved, and a parameter study of some key parameters were conducted to determine how they influenced the possible amount of layers in a stacked DE. In this present work, we wish to extend our previous model to also include the effect of the mechanical deformation of a multilayered stack of DEs. With this electro-thermal and -mechanical (ETM) model, a parameter study will be conducted to examine the effect of some key operating as well as geometric parameters. The results will be compared to the previous ET model, to investigate the effect of mechanical deformation on the possible amount of layers in a stack. Furthermore, three different hyperelastic material models, used to model the elasticity of the elastomer layer, will be compared, in order to investigate how the choice of material model influences the breakdown point.

Types of Breakdown

As depicted in Figure 2, several types of electrical ageing mechanisms occur in DEs. The slow degradation mechanisms form electrical and water trees that break down the material over significant time scales, i.e. 15 minutes and above, from initiation of the ageing mechanism, to full material breakdown[18,20]. Furthermore, the degradation mechanisms are low-level, meaning that the required electric field for breakdown to occur is low.

The breakdown mechanisms occur at time scales much lower than for degradation mechanisms, and they are somewhat instantaneous. Partial discharge can lead to a DE breaking down if the elastomer layer is thin. However, if the elastomer is thick or multiple layers are stacked, it is more likely that partial discharge leads merely to the formation of electrical trees and *not* instantaneous breakdown[18,19]. Electrical breakdown occurs due to an exponential increase in electrical carriers, where new carriers are created when existing carriers with high kinetic energy collide with the elastomer matrix[18]. Several studies have been conducted in order to study electrical breakdown in DEs[23,29–32].

The electromechanical breakdown of DEs occurs because the mechanical compressive force caused by the electrostatic attraction of the electrodes is greater than the elastic

force of the elastomer, which consequently results in a snap-through of the material[18]. This snap-through may either be local or macroscopic, but most often it is a local snap-through caused by irregularities on the surface of the elastomer. If the DE is operated with constant applied voltage, a thinning of the material will result in an increased electric field, which in turn causes more thinning of the material, and eventually result in electromechanical breakdown. Several studies have been conducted to study the electromechanical instability of DEs, both experimentally and model-based[30–37].

The thermal breakdown of DEs occurs due to an exponential increase in temperature within the stack, because the thermal energy generated within the stack cannot be balanced by heat loss on the surface[18]. The thermal energy generated within the stack is mainly due to Joule heating of the material, i.e. heating due to electrical resistance in the material. The amount of Joule heating generated pr. volume, q, in a multilayered DE with N layers, each with an initial thickness of d, and an active cross-sectional area A is determined by Joule's law:

$$q = \frac{V^2}{R\,N\,d\,A} = E^2\sigma \tag{1}$$

where V is the applied voltage over one elastomer layer, R the electrical resistance of the material, E the applied electric field, and σ the electrical conductivity of the elastomer. It is most relevant to consider thermal breakdown when using stacked DEs, since in this case multiple layers lead to an increase in volume, and consequently more Joule heating will occur without a corresponding increase in surface area. Thus, heat lost into the surroundings can no longer balance the heat generated within the stack.

Model Setup

As already mentioned, thermal breakdown is particularly important when considering a multilayered DE. Therefore, the configuration used throughout this work is a cylindrical stack of N layers of DEs placed on top of each other, with alternating electrode and elastomer layers. The configuration has an active and an inactive part, with the active

part being that where the electrodes are placed. Furthermore, the active part has a radius of R_{A} and the inactive part has a radial width of R_{I}, as shown in Figure 3. Each elastomer layer has a thickness d before any actuation takes place. The electrode layers are approximately three orders of magnitude thinner than the elastomer layers, and thus it is assumed that they do not influence the mechanical properties of the DE. Furthermore, the thermal conductivity of the conductive electrode material is much higher than that of the elastomer material, and hence they dissipate heat away much faster than the elastomer layers. It is therefore assumed that the electrode layers are not the cause for thermal breakdown, and thus both the mechanical and thermal effects of the electrode layers are neglected.

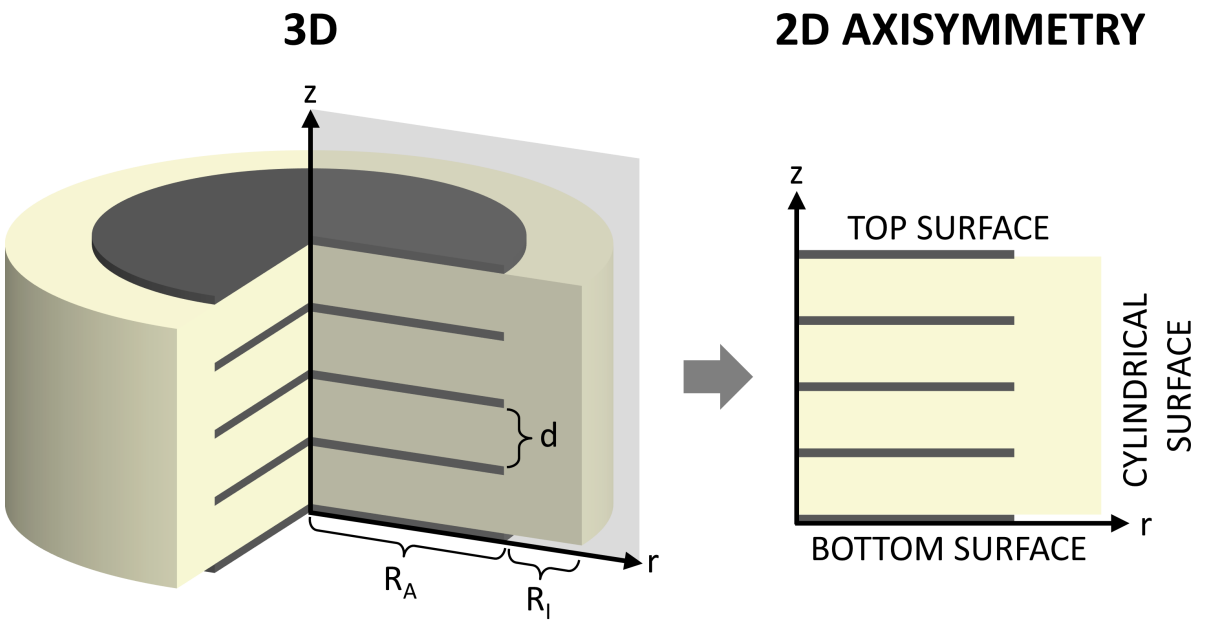

Figure 3: The configuration used throughout this work is a cylindrical stack with N layers of elastomer, each with a thickness of d. The active part of the stack, and thus the part with electrodes, has a radius of R_{A}, and the inactive part of the stack has a radial width of R_{I}. Due to symmetry, the actual 3D geometry of the stack may be modelled as a 2D axisymmetric geometry.

The elastomer material simulated in this work is a polydimethylsiloxane (PDMS) elastomer, specifically Bluestil RTV 141 from Blustar Silicones[39], with a thermal conductivity of $k = 0.16$ W/(mK) and a relative permittivity of $\epsilon_r = 2.7$[39]. In our previous work[38], we found that the electrical conductivity of the PDMS elastomer could be described by

an Arrhenius expression with respect to temperature T:

$$\sigma_{\mathrm{Arr}}(T) = \sigma_{0,\mathrm{Arr}} \exp\left(-\frac{\beta_{\mathrm{Arr}}}{T}\right) = 1.261 \cdot 10^{-5}\ \mathrm{S\ m^{-1}} \cdot \exp\left(-\frac{5968\mathrm{K}}{T}\right) \tag{2}$$

It should be noted that in Christensen et. al[38], the material used to determine σ_{Arr} was also a PDMS elastomer, but specifically Elastosil RT625 from Wacker Chemie AG. However, it is assumed that Bluesil RTV 141 follows a similar Arrhenius-type equation with respect to temperature, since the two elastomers are very similar with respect to composition. Thus Eq. 2 is used for the electrical conductivity. The hyperelastic material models used to describe the mechanical behaviour of the elastomer material are the Gent, Mooney-Rivlin, and Ogden models, and these will be described in more detail in the coming chapter.

The geometry is implemented into the commercial finite-element-method (FEM) software COMSOL Multiphysics®, where it is utilised that the multilayered stack of DEs is 2D axisymmetric, as seen in Figure 3, and thus a stationary 2D axisymmetric model is set up. The modules used in COMSOL Multiphysics® are the "Electromechanics" module, which combines the modules "Solid Mechanics" and "Electrostatics" with the multiphysics module "Electromechanical Forces", and the "Heat Transfer in Solids" module, all of which combine to form the ETM model.

In the "Structural Mechanics," module the hyperelastic material model of the elastomer is specified (as elaborated in the coming chapter), and it is specified that the bottom surface is restricted from moving in the z-direction, though it is still free to extend or compress in the r-direction. In the "Electrostatics" module, it is merely specified that every second electrode is a ground electrode, and every other electrode is a terminal with an applied voltage V.

Natural convection takes place along all external surfaces of the stack, and natural convection on a given surface, h, is given by the following expression[40]:

$$h(T) = h_0 \left(T - T_0\right)^{1/4} \tag{3}$$

where h_0 is the heat transfer coefficient of that surface, T the temperature at that surface, and T_0 the ambient temperature of the surrounding air. However, Eq. 3 is not differentiable at $T = T_0$, which causes problems when implementing this equation into COMSOL Multiphysics®. Therefore, a small modification is implemented into Eq. 3 to make it differentiable at all points:

$$h(T) = h_0 \cdot \left[(T - T_0)^2 \mathrm{K}^{-1} + 1 \right]^{1/8} \tag{4}$$

Eq. 4 is implemented as the heat flux on all surfaces of the stack of DEs in the "Heat Transfer in Solids" module. The heat transfer coefficients are $h_{0,\mathrm{t}} = 2.44$ W/(m^{2}K), $h_{0,\mathrm{b}} = 1.31$ W/(m^{2}K), and $h_{0,\mathrm{c}} = 1.97$ W/(m^{2}K) for the top, bottom and cylindrical surfaces, respectively[40]. In the "Heat Transfer in Solids" module, a heat source that generates Joule heating, as given by Eq. 1, is furthermore specified.

The base case geometry of the model has an active part with a radius $R_\mathrm{A} = 50$ cm, and no inactive part, thus $R_\mathrm{I} = 0$ cm, and each elastomer layer has an initial thickness of $d = 50$ μm. The applied voltage is $V = 3.5$ kV, and the ambient temperature is $T_0 = 15^\circ$C in the base case. From this base case, one parameter will be varied while keeping the remaining constant when performing the parameter studies.

Figure 4 shows the results from simulating the base case with $N = 4000$ layers and using the Gent hyperelastic material model for simulating the mechanical behaviour of the elastomer. The resulting electric field within the stack is uniform and has a magnitude of $E = 84.7$ V/μm, and the stretch ratio in z-direction is $\lambda_z = 0.83$. The initial geometry of the stack is outlined with the black contour line, while the simulated displacement of a given point is shown with the rainbow-coloured scale on the right open-faced surface of the stack. As seen in the figure, displacement increases gradually from no displacement at the bottom centre point, to maximum displacement at the top right point. The left open-faced surface of the stack displays the temperature within the stack, and the point with the highest temperature is identified. The hotspot of the base case stack is located at $r_\mathrm{HS} = 0$ cm and $z_\mathrm{HS} = 0.45\,N\,d$, thus at the radial centre, while only at 45% of the height of the stack due to differences in heat transfer coefficients between the top and

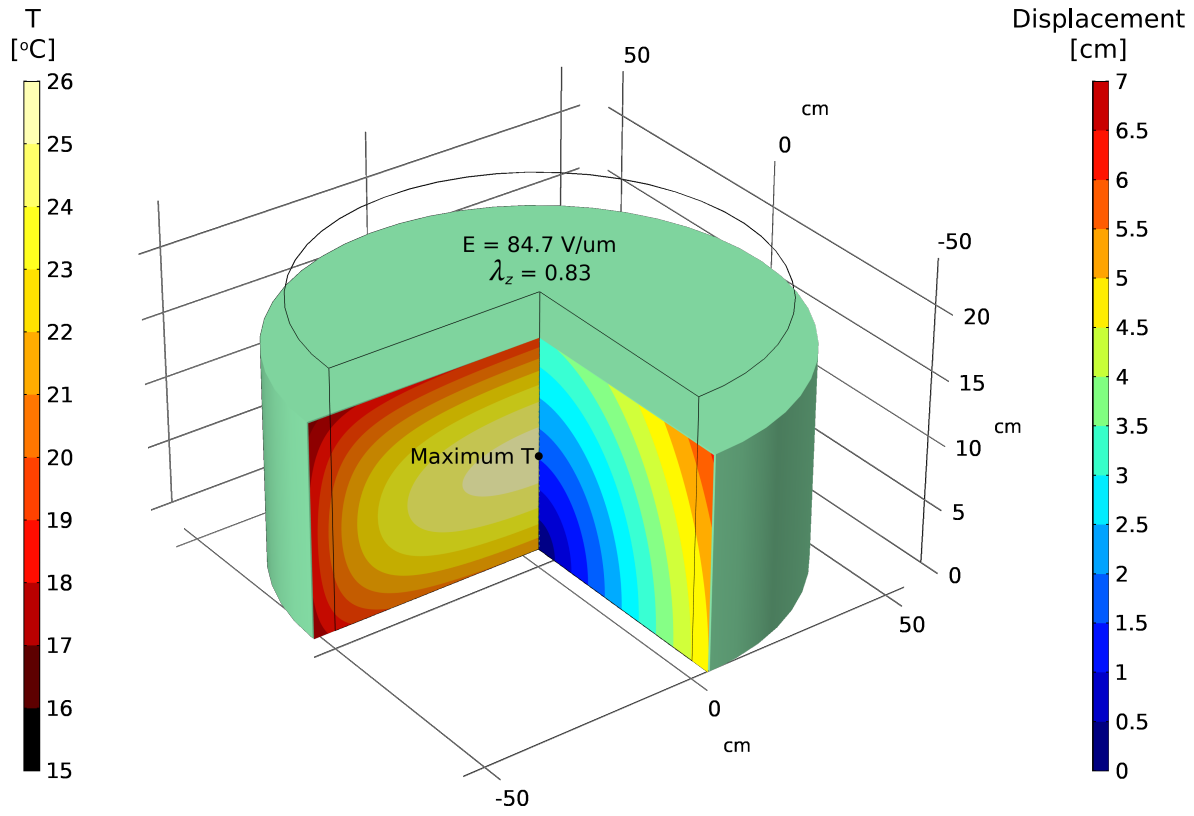

Figure 4: Simulation of the base case with N = 4000 layers. The stack has R_{A} = 50 cm, R_{I} = 0 cm, and d = 50 μ. Furthermore, V = 3.5 kV and T_0 = 15°C. The resulting uniform electric field in the stack is E = 84.7 V/μm, and the stretch ratio is λ_z = 0.83. The left open-faced surface of the stack displays the temperature in °C within the stack, and the point with the highest temperature is identified. The initial geometry of the stack is displayed by the black contoured line, and the right open-faced surface of the stack displays the resulting displacement of a given point in cm.

bottom surfaces of the stack.

Besides varying the parameters already introduced, a parameter study with a high electrical conductivity particle in the DE stack is also conducted. This particle is introduced in order to simulate an impurity in the material, and it is placed in the hotspot of the stack with a given particle radius R_{par}. The electrical conductivity of the particle is σ_{par}, and it is also assumed to follow an Arrhenius expression with respect to temperature.

Material Models

To model the mechanical deformation of the stack of DEs, a material model that describes the nonlinear stress-strain relationship of the elastomer is required, and so three well-known hyperelastic material models are compared in this study.

The first model is the two-parameter Gent model, W_{G}, which is very common in

the field of DEs due to its ability to account for elastomer strain-hardening[41–43]. The second option in this study is the widely used Mooney-Rivlin model, W_{MR}, which is a simple two-parameter model[41]. The third and last model is the versatile Ogden model, W_{O}, which, with its six-parameters, is able to fit almost any experimental data[41,44]. The hyperelastic constitutive equations are as follows[41,43]:

$$W_{\mathrm{G}} = -\frac{Y}{6} J_{\mathrm{m}} \ln\left(1 - \frac{I_1 - 3}{J_{\mathrm{m}}}\right) \tag{5}$$

$$W_{\mathrm{MR}} = C_1 (I_1 - 3) + C_2 (I_2 - 3) \tag{6}$$

$$W_{\mathrm{O}} = \sum_{i=1}^{3} \frac{\mu_i}{\alpha_i} \left(\lambda_1^{\alpha_i} + \lambda_2^{\alpha_i} + \lambda_3^{\alpha_i} - 3\right) \tag{7}$$

where W is strain energy density, I_1 and I_2 the first and second strain invariants, and λ_i the stretch ratio in the i^{th} direction. As already mentioned, the Gent strain energy density model in Eq. 5 contains two parameters, namely Y, which is the Young's modulus, and J_m, which correlates with the maximum stretch of the elastomer and must always obey $I_1 < J_{\mathrm{m}} + 3$[43]. The Mooney-Rivlin strain energy density model in Eq. 6 contains the two empirical parameters, C_1 and C_2, and the Ogden strain energy density model in Eq. 7 contains the six empirical parameters, μ_i and α_i with $i = 1, 2, 3$.

Meunier et al.[41] conducted a thorough study in which they measured stress as a function of stretch using Bluesil RTV141 under various mechanical loadings. Subsequently, they fitted several hyperelastic constitutive equations to the data, thus using data from all different mechanical loadings. The values of the fitted parameters for the hyperelastic material models of interest to this work are shown in Table 1, and these values will be used throughout this work.

Table 1: Values of fitted parameters in hyperelastic constitutive equations, Eq. 5-7. Model fitting performed by Meunier et al.[41].

Models	Parameters		
Gent	Y = 970 kPa	J_{m} = 13	
Mooney-Rivlin	C_1 = 140 kPa	C_2 = 23 kPa	
Ogden	μ_1 = 460 kPa	μ_2 = 0.27 kPa	μ_3 = −7.4 kPa
	α_1 = 1.4	α_2 = 10	α_3 = −3.3

Figure 5 displays the stretch ratio as a function of applied mechanical force, F, during uniaxial compression of Bluesil RTV141 when using the three different hyperelastic models. From the figure, it is evident that all three models are equal until $F \approx 10$ N/mm^2, and from that point onwards the Gent model strain hardens, whereas the Mooney-Rivlin and Ogden models continue to thin the elastomer, albeit at different rates.

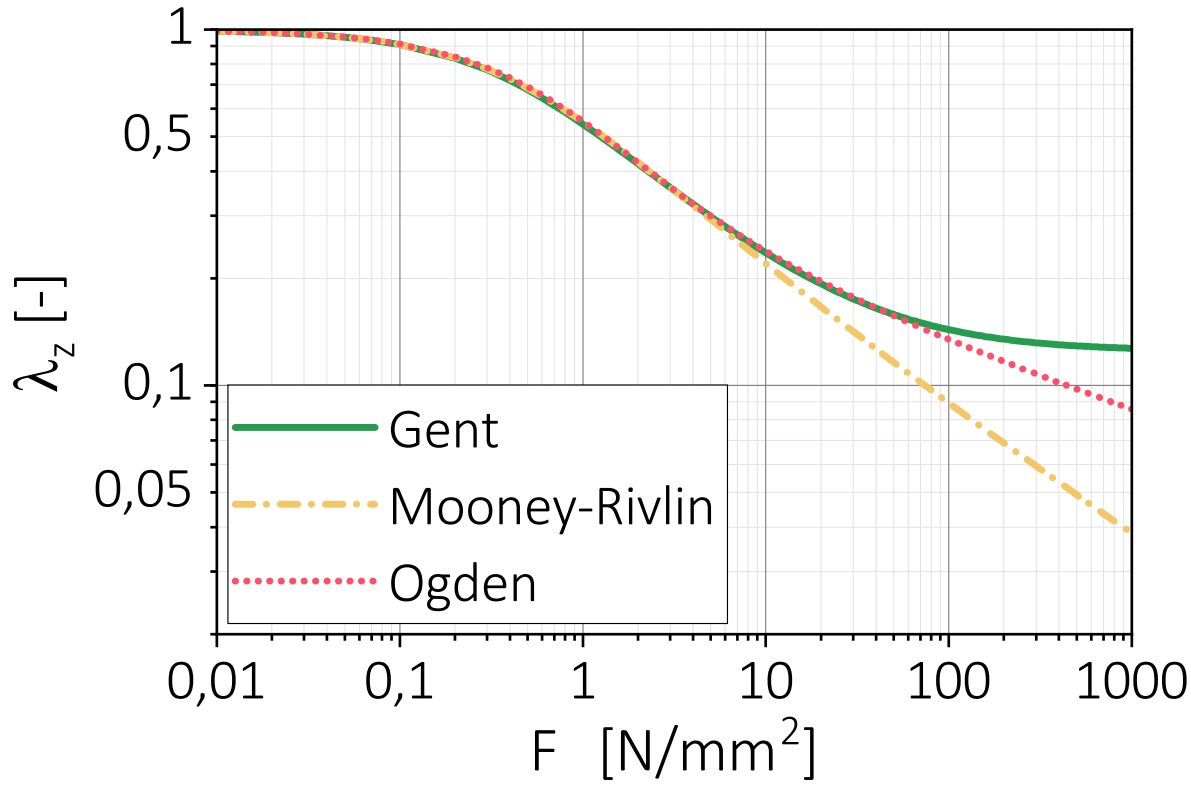

Figure 5: Stretch ratio as a function of the applied mechanical force of the elastomer material when using three different hyperelastic material models.

Parameter Study

A parameter study is conducted in which it is examined how many layers it is possible to stack in a multilayered DE before thermal breakdown occurs, N_{BD}, when varying one given parameter from the base case while maintaining the remaining parameters. As stated previously, the base case geometries in this work are $R_{\mathrm{A}} = 50$ cm and $R_{\mathrm{I}} = 0$ cm, and base case operating conditions are $V = 3.5$ kV and $T_0 = 15^{\circ}$C. Furthermore, three different hyperelastic material models for the elastomer material in the ETM model are compared, as well as compared to the pure ET model – hence the case with Joule heating

but no mechanical deformation, as specified in Christensen et al[38].

Active Part

The active part of the DE stack is covered by electrodes, as seen in Figure 3. When increasing R_A, it is evident from Figure 6a that N_{BD} decreases significantly, both for the ET model and all three ETM models. This may be explained by the fact that an increase in R_A leads to an increase in the volume and thus the amount of Joule heating in the stack. Of course, the surface area of the stack also increases with R_A, though not enough to balance the excess heat generated, which results in thermal breakdown occurring at a lower amount of layers.

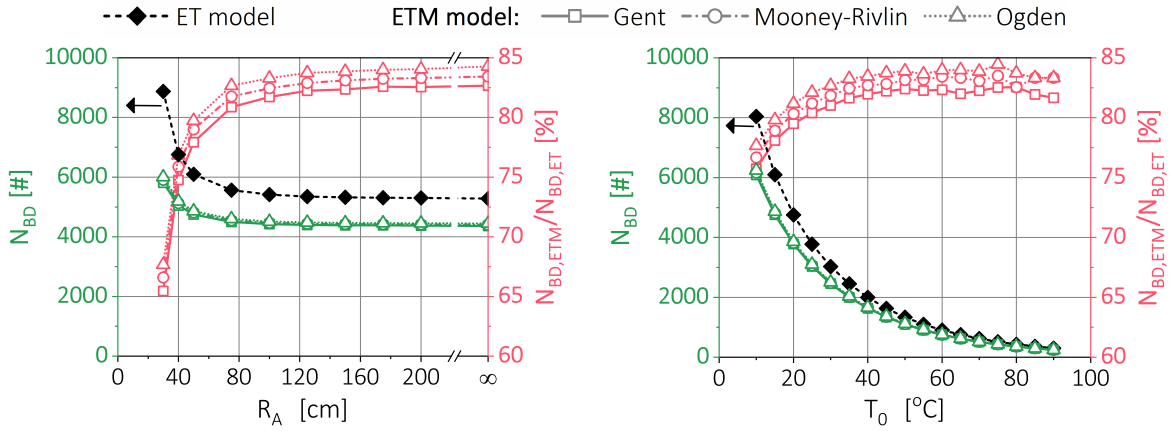

(a) Radius of the active part of DEs, R_A.

(b) Ambient temperature of the surrounding air, T_0.

Figure 6: Parameter study of (a) R_A and (b) T_0. Left y-axis: N_{BD} of results from the pure ET model, as well as ETM models with all three different hyperelastic material models. Right y-axis: ratio between $N_{BD,ETM}$ for the relevant ETM model and $N_{BD,ET}$ for the ET model.

As R_A approaches infinity, N_{BD}, for both the ET model as well as all three ETM models, asymptotically approaches different plateaus. For the ET model, the plateau value is $N_{BD,ET}(R_A = \infty) = 5280$, and for the ETM models the plateau values are $N_{BD,ETM}(R_A = \infty) = 4365 - 4450$, depending on the utilised material model. $R_A = \infty$ is equivalent to having thermal insulation on the cylindrical surface of the stack, thus no heat dissipation occurs in the r-direction. On the contrary, as $R_A \to 0$, then theoretically $N_{BD} \to \infty$, since the ratio of surface area to volume approaches infinity. This means that the dissipated heat at the surface of the stack is always able to balance the generated Joule heating within the stack when R_A is small enough.

When comparing the results for the three ETM models with the results from the ET model, it is clear that the difference in N_{BD} is significant, with the ratio between $N_{\mathrm{BD,ETM}}$ and $N_{\mathrm{BD,ET}}$ being 65-85%. This is expected, because when electro-mechanical deformation is included in the model, the actual electric field in the stack is much higher than that based on the applied voltage, and thus more Joule heating is generated based on Eq. 1. It should be noted furthermore that the chosen hyperelastic material model for the elastomer has an influence on N_{BD}, although this is minimal. The Gent model is the most restrictive model with respect to predicting N_{BD}, and the Ogden model is the least restrictive model, and the difference in N_{BD} values as predicted by the two models varies between 195 layers at $R_{\mathrm{A}} = 30$ cm and 85 layers at $R_{\mathrm{A}} = \infty$.

Ambient Temperature

The ambient temperature of the surrounding air has a huge impact on N_{BD} for both the ET model and the ETM models, as seen in Figure 6b, as N_{BD} significantly decreases when increasing T_0. For the ET model, a decrease of 7740 layers in $N_{\mathrm{BD,ET}}$, from $T_0 = 10^{\circ}$C to $T_0 = 90^{\circ}$C, is calculated. For the ETM models, the reductions in N_{BD} from $T_0 = 10^{\circ}$C to $T_0 = 90^{\circ}$C are 5845 layers for Gent, 5915 layers for Mooney, and 5995 layers for Ogden. The reason for the huge decreases in N_{BD} when increasing T_0 is the limitations in natural convection on the surfaces of the stack. The driving force for removing excess heat at the surfaces of the stack is the difference between T_0 and the temperature on the surface, as seen in Eq. 4. Thus, when T_0 increases, less heat is transported away on the surface of the stack, and the temperature within the stack raises, which leads to lower N_{BD}.

When comparing $N_{\mathrm{BD,ET}}$ and $N_{\mathrm{BD,ETM}}$, it may appear that the results from the ET model and ETM models come close to matching when increasing T_0. However, by looking at the ratio between $N_{\mathrm{BD,ETM}}$ and $N_{\mathrm{BD,ET}}$, it is evident that this ratio only increases slightly with T_0, thus more or less maintaining the relative difference between the results of the models. It should again be noted that $N_{\mathrm{BD,ET}}$ is in any case larger than $N_{\mathrm{BD,ETM}}$, because when including electro-mechanical deformation, the actual electric field within the stack is larger than that predicted by the initially applied voltage, consequently

leading to more Joule heating in the stack.

The choice of hyperelastic material model for the elastomer in the ETM model has the greatest impact at low temperatures, since the differences between N_{BD} predicted by the three different models are 155 layers at T_0 = 10°C, while only a difference of 5 layers at T_0 = 90°C, with the Gent model being the most restrictive one, and the Ogden model being the least restrictive. However, when looking at the relative difference between the Gent and the Ogden model over the entire temperature span, the N_{BD} values predicted by the Ogden model are approximately 2% greater than those predicted by the Gent model, while those predicted by the Mooney-Rivlin model are approximately 1% greater than those predicted by the Gent model.

Applied Voltage

The next parameter studied herein is the applied voltage, V, and the results are shown in Figure 7. From Figure 7a, it is evident that N_{BD} decreases in line with increasing V, which from Eq. 1 may be ascribed to the fact that more Joule heating occurs when the applied voltage increases.

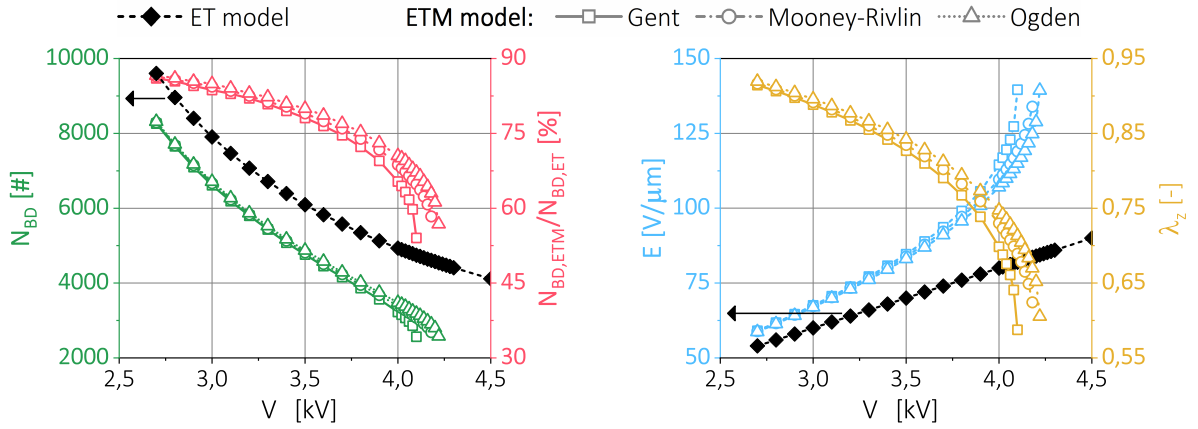

(a) Left y-axis: N_{BD} as a function of varying V for both the ET model and all three ETM models. Right y-axis: ratio of $N_{\mathrm{BD,ETM}}$ for the given ETM model and $N_{\mathrm{BD,ET}}$ for the ET model.

(b) Left y-axis: Effective electric field in the stack, E, as a function of the applied voltage for both the ET and ETM models. Right y-axis: stretch ratio of the stack, λ_z, for each of the ETM models.

Figure 7: Parameter study of applied voltage, V.

Using the Gent hyperelastic material model to model the mechanical behaviour of the elastomer yields the lowest N_{BD} values when comparing it to the other two ETM models, whereas using the Ogden hyperelastic material model results in the highest N_{BD} values of

the three ETM models. The difference in N_{BD} for the Gent and Ogden models increases from 50 layers at V = 2.5 kV to 625 layers at V = 4.1 kV. However, the results from all the ETM models yield lower N_{BD} values than those of the ET model at all values of V, which again can be ascribed to the fact that no electro-mechanical deformation occurs in the ET model. Furthermore, when looking at the ratio of $N_{\mathrm{BD,ETM}}$ to $N_{\mathrm{BD,ET}}$, it is evident that the difference between the ET and ETM models increases with the applied voltage, due to more compression occurring in the ETM models, as seen on the right y-axis in Figure 7b.

One additional thing to note from Figure 7a is that it was not possible to achieve any steady-state results for the Gent model above V = 4.1 kV, for the Mooney-Rivlin model above V = 4.18 kV or for the Ogden model above V = 4.22 kV, no matter how small an increment in V was used. However, no maximum V for the ET model was observed. A possible explanation for these observations in the ETM models is that above these values of V, no stable solution can be found, because electro-mechanical breakdown of the DE stack occurs, which, as described previously, occurs because the electrostatic forces increase the elastic forces of the elastomer. The left y-axis in Figure 7b displays the effective electric field in the stack, E, when increasing V, and as can be seen, the slope of $E = f(V)$ approaches infinity, thereby indicating that the electrostatic forces increase to infinity as well. Furthermore, from the right y-axis in Figure 7b, it is notable that the stretch ratio in the z-direction, λ_z, also decreases rapidly in line with increasing V and that the slope $\partial\lambda_z/\partial V \rightarrow -\infty$, indicating catastrophic thinning of the stack.

Inactive Part

In this section, the influence of having an inactive area with a given radial width, R_{I}, as illustrated in Figure 3, is studied. In Figure 8a, we see that in general there is little influence on N_{BD} by having an inactive part in the DE stack. However, the trend of N_{BD} when varying R_{I} depends on the R_{A}-value.

When including an inactive area in the DE stack it will cause some mechanical restrictions on the active part yielding a non-uniform electric field, E, as well as a non-uniform

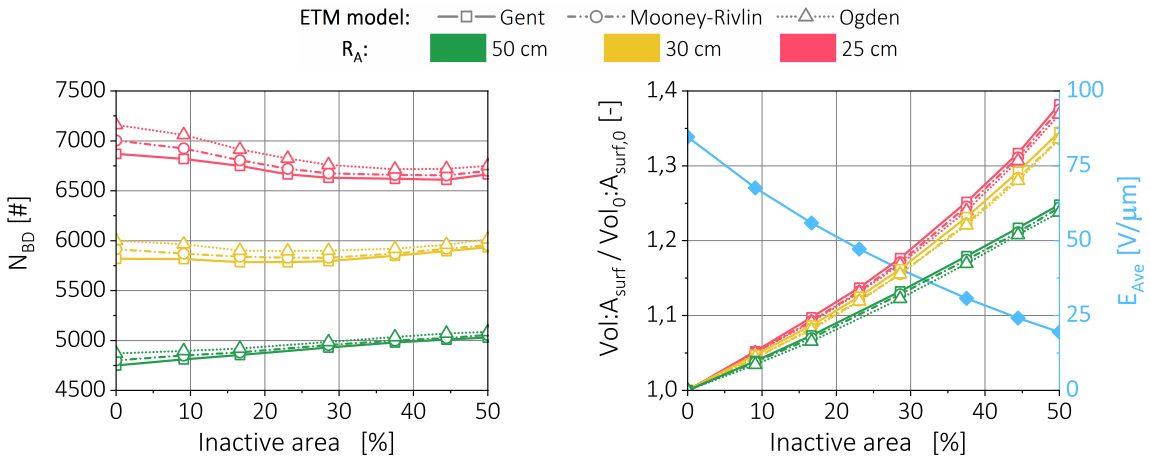

(a) N_{BD} as a function of percentage inactive area.

(b) Left y-axis: Ratio of Vol:$\mathrm{A_{surf}}$ to $\mathrm{Vol_0}$:$\mathrm{A_{surf,0}}$ as a function of percentage inactive area. Right y-axis: Average electrical field, E_{Ave}, in the stack as a function of percentage inactive area.

Figure 8: Parameter study examining the effect of having an inactive area of radial width R_{I} in the stacked DE, as illustrated in 3. The results at three different R_{A} values and for all three ETM models are compared.

stretch ratio, λ_z, of the stack, as seen in Figure 9. The simulations shown in Figure 9 use the Gent hyperelastic model; however, the trends are similar for simulations with the Mooney-Rivlin and the Ogden hyperelastic models. The average value of E and λ_z in a stack with an inactive area will therefore be lower and higher, respectively, than in the corresponding stack without an inactive area. The right y-axis in Figure 8b shows how the average electric field, E_{Ave}, of the stack decreases in line with an increasing inactive area. A lower electric field causes less Joule heating, and thus more layers can be stacked before thermal breakdown occurs. However, when adding an inactive area to a stack, the volume-to-surface-area-ratio, Vol:$\mathrm{A_{surf}}$, increases and this introduces limitations in heat dissipation; consequently, the temperature in the stack increases and fewer layers can be stacked before thermal breakdown occurs. These two mechanisms compete when studying how N_{BD} changes as a function of adding an inactive area.

The left y-axis in Figure 8b displays the ratio of Vol:$\mathrm{A_{surf}}$ to $\mathrm{Vol_0}$:$\mathrm{A_{surf,0}}$ as a function of the percentage of inactive area. Vol:$\mathrm{A_{surf}}$ is the volume-to-surface-area ratio at a given R_{A} and percentage of inactive area, and $\mathrm{Vol_0}$:$\mathrm{A_{surf,0}}$ is the volume-to-surface-area ratio at the same R_{A} but 0% inactive area. From the figure, it is notable that the ratio increases the most when increasing the inactive area at R_{A} = 25 cm, and the least when R_{A} = 50 cm. Consequently, limitations in heat transfer are most significant when R_{A} = 25 cm, and

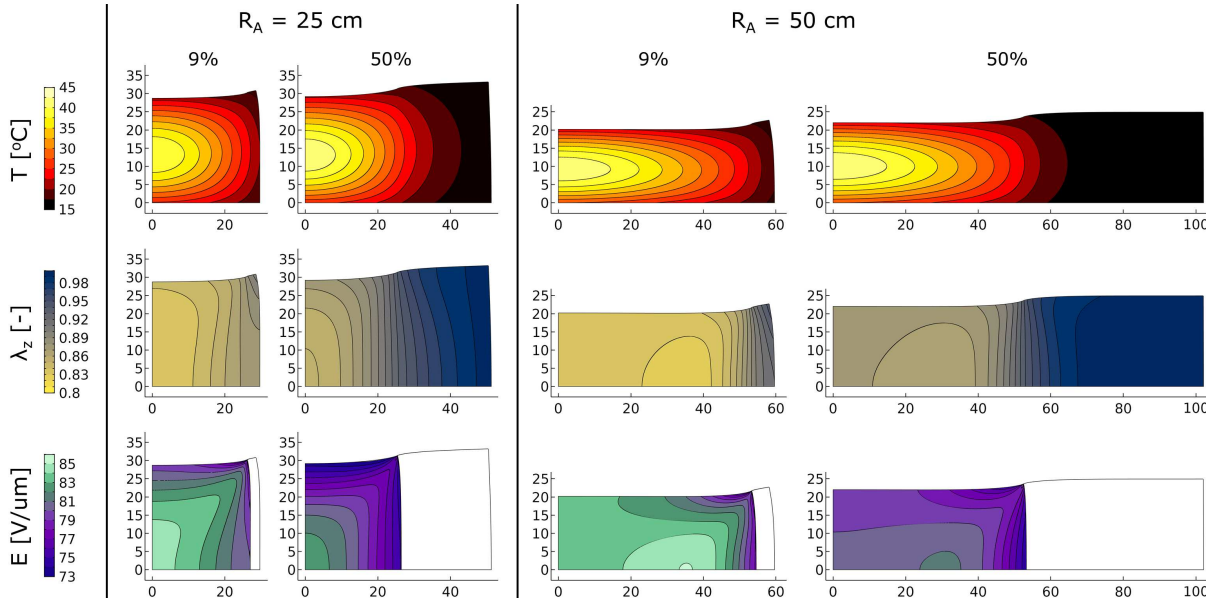

Figure 9: Simulations showing the temperature T, stretch ratio λ_z, and electric field E within DE stacks with R_A = 25 cm and R_A = 50 cm, and with 9% and 50% inactive area, respectively. Simulations shown here are performed using the Gent hyperelastic model, but similar trends are observed for results using the Mooney-Rivlin and Ogden models. The number of layers in each simulation is equal to N_BD for the given geometry.

they become increasingly less important as R_A increases. Limitations in heat transfer thus explain the decrease in N_BD when increasing the inactive area for a DE stack measuring R_A = 25 cm. Conversely, mechanical limitations yielding lower electric fields and less Joule heating dominate when R_A = 50 cm, which explains the increase in N_BD in line with an increasing inactive area. When R_A = 30 cm, there is little influence on N_BD when the inactive area increases, because the two mechanisms roughly cancel each other out.

The trends for N_BD when varying the inactive area at a given R_A are similar for all three ETM models. However, in all cases, the results obtained using the Ogden model predict the highest breakdown point, and results using the Gent model yield the most restrictive estimation of the breakdown point, which is consistent with what was observed in the previous parameter studies of R_A, T_0, and V.

Figure 9 shows T, λ_z, and E in DE stacks with R_A = 25 cm and R_A = 50 cm and 9% and 50% inactive areas, respectively. The numbers of layers in the stack are $N = N_\mathrm{BD}$ for the given R_A and R_I. The simulations are performed using the Gent hyperelastic model, albeit similar trends are observed for simulations with the Mooney-Rivlin and Ogden models. As already mentioned, it is evident that when including an inactive area in the

DE stack, non-uniform E and non-uniform λ_z are achieved, and so regions with a high electrical field and a low λ_z appear, resulting in more Joule heating occurring in these regions. From Figure 9 it should be noted furthermore that the major part of the inactive area has a negligible electric field, and thus no Joule heating occurs in these regions.

When increasing the inactive area of the DE stack, increasingly more mechanical restrictions are imposed on the active area, as can be seen by the increase in the stretch ratio which in turn induces a decrease in the electric field. It should be noted that when $R_{\mathrm{A}} = 50$ cm, the region with the lowest stretch ratio, hence most compression and highest electrical field, is not located at the centre at the stack but rather at a region closer to the inactive area.

The temperature profiles of the stacks maintain the same overall outline as for those cases without inactive areas, even when local regions with a high electric field appear. As a result, no local hotspots in those regions appear, which indicates that heat dissipation within the stack is able to distribute the excess heat generated in regions with higher electric fields.

High Conductivity Particle

The majority of the predicted values of N_{BD} have been in the order of $N_{\mathrm{BD}} = 2000 - 10000$ layers, with the only exceptions being at high ambient temperatures. This is far beyond the maximum amount of layers currently seen in DE applications; for example, SBM Offshore has built a wave energy harvester with a maximum of 300 layers[9]. One explanation for the differences in N_{BD}-values is it that up until this point, the simulated elastomer material has been a perfect material with no imperfections or impurities, which is a crude approximation. During fabrication of a DE, there are multiple steps where dust or other airborn particles may be trapped in the DE, as captured by Araromi et al.[45]. Dust particles have sizes between 0.5 μm and 10 μm[46,47], but when working in a cleanroom, which is often the case when fabricating DEs, the majority of particles in the region of $> 5\,\mu$m are removed[48].

Therefore, a parameter study in which a single particle with radius $R_{\mathrm{par}} = 1, 2, 5\,\mu$m

placed in the hotspot of the DE stack is conducted. The particle is placed in the hotspot of the stack in order to simulate the worst-case scenario with respect to location of an entrapped particle. It is most likely that the trapped particle has higher conductivity than the elastomer material in which it is entrapped, and thus it is assumed that its electrical conductivity, σ_{par}, follows an Arrhenius type expression similar to the one given in Eq. 2, only with an increased $\sigma_{0,\text{Arr}}$.

The relative location of the hotspot in the DE stack without any entrapped particle, $z_{\text{HS}}/z_{\text{max}}$, is a function of the number of layers, as seen in Figure 10a. $z_{\text{HS}}/z_{\text{max}}$ is the ratio between the z-coordinate at the hotspot of the stack and the maximum z-coordinate, hence the height of the stack after deformation. It was found that the relative location of the hotspot perfectly obeys the following empirical relationship with the number of layers in the stack, N:

$$\frac{z_{\text{HS}}}{z_{\text{max}}} = 7.2 \cdot 10^{-13} N^3 - 9.7 \cdot 10^{-9} N^2 + 5.4 \cdot 10^{-5} N + 0.35 \tag{8}$$

Thus, the above equation is used to determine the z-coordinate of the particle, and the r-coordinate of the hotspot, r_{HS}, and the particle is $r_{\text{par}} = r_{\text{HS}} = 0$ cm at all values of N.

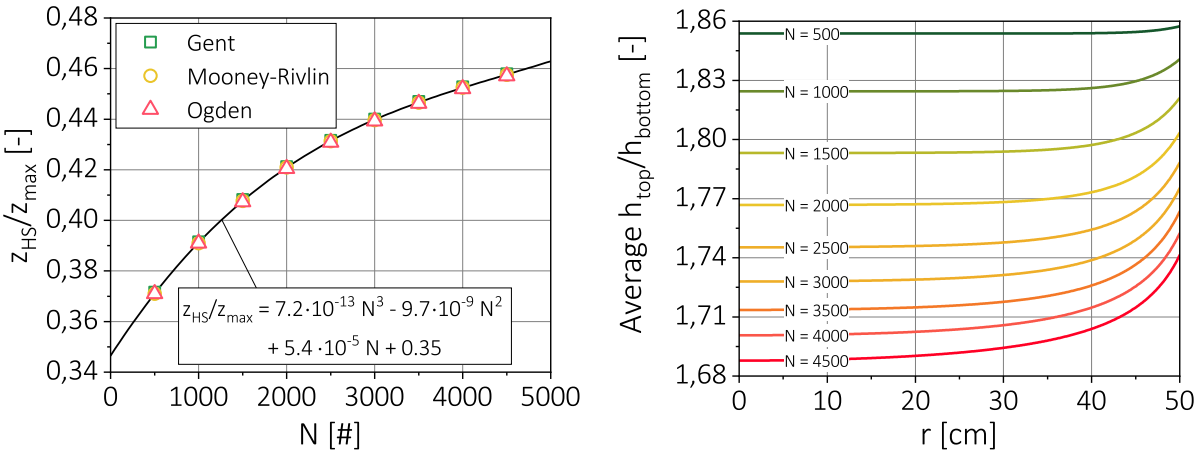

(a) Relative location in the z-direction of the hotspot, $z_{\text{HS}}/z_{\text{max}}$, in the stacked DE as a function of the number of layers, N.

(b) Ratio of $h_{\text{t}}/h_{\text{b}}$ averaged for all three ETM models, as a function of the R-coordinate and at various values of N.

Figure 10: Study of the placement of the hotspot in a multilayered DE with $R_{\text{A}} = 50$ cm.

The reason why the relative location of the hotspot changes is that when N increases, the average temperature of the stack increases as well, which in turn causes the amount

of natural convection occurring at the top and the bottom of the stack to increase. The equation for natural convection is given in Eq. 3, with $h_{0,t}$ = 2.44 W/(m^{2}K) and $h_{0,b}$ = 1.31 W/(m^{2}K) for the top and the bottom, respectively. Figure 10b displays the ratio between $h_{\mathrm{t}}(T)/h_{\mathrm{b}}(T)$, averaged over all three ETM models, as a function of the r-coordinate, and at various values of N. It can be seen from the figure that the ratio h_t/h_b decreases towards 1 when N increases, which means that the amount of heat dissipated away at the top and bottom equalizes slightly, and thus the relative location of the hotspot approaches the middle of the stack.

Figure 11a shows the resulting N_{BD} of the DE stack with an entrapped particle as a function of σ_{par} at 15°C at various R_{par}-values. As evidenced in the figure, N_{BD} decreases rapidly in line with increasing conductivity of the particle, due to more Joule heating occurring as σ increases (see Eq. 1). The results shown at approximately $\sigma_{\mathrm{par}} = 10^{-14}$ S/m correspond to the case with no particle in the stack. A simulated temperature profile of the stack with $R_{\mathrm{par}} = 5\,\mu$m, $N = 1300$, $\sigma_{\mathrm{par}} = 6.38 \cdot 10^{-5}$ S/m, and using the Gent hyperelastic model, is shown in Figure 11b. From the temperature profile, it is clear that the stack's hotspot is located directly in the same location as the particle, and that the temperature in the close vicinity of the particle is significantly higher than in the bulk DE. When comparing this temperature profile to that of the base case in Figure 4, it is clear that the presence of the single particle in the stack is the cause of thermal breakdown.

When the diameter of the particle increases from $R_{\mathrm{par}} = 1\,\mu$m, to $R_{\mathrm{par}} = 2\,\mu$m, to $R_{\mathrm{par}} = 5\,\mu$m, the maximum value of σ_{par} at which it is possible to achieve a steady-state solution decreases significantly. This is due to the fact that a bigger particle with high electrical conductivity yields more Joule heating, and thus a lower value of σ_{par} is achievable before thermal breakdown occurs therein. For the particle with $R_{\mathrm{par}} = 1\,\mu$m, the maximum achievable value was approximately $\sigma_{\mathrm{par}} = 8 \cdot 10^{-3}$ S/m, for $R_{\mathrm{par}} = 2\,\mu$m the maximum value was $\sigma_{\mathrm{par}} = 1 \cdot 10^{-3}$ S/m and for $R_{\mathrm{par}} = 5\,\mu$m the maximum achievable value was $\sigma_{\mathrm{par}} = 6.5 \cdot 10^{-5}$ S/m. Thus, a five-fold increase in the particle radius yields an decrease in the maximum σ_{par} of two orders of magnitude.

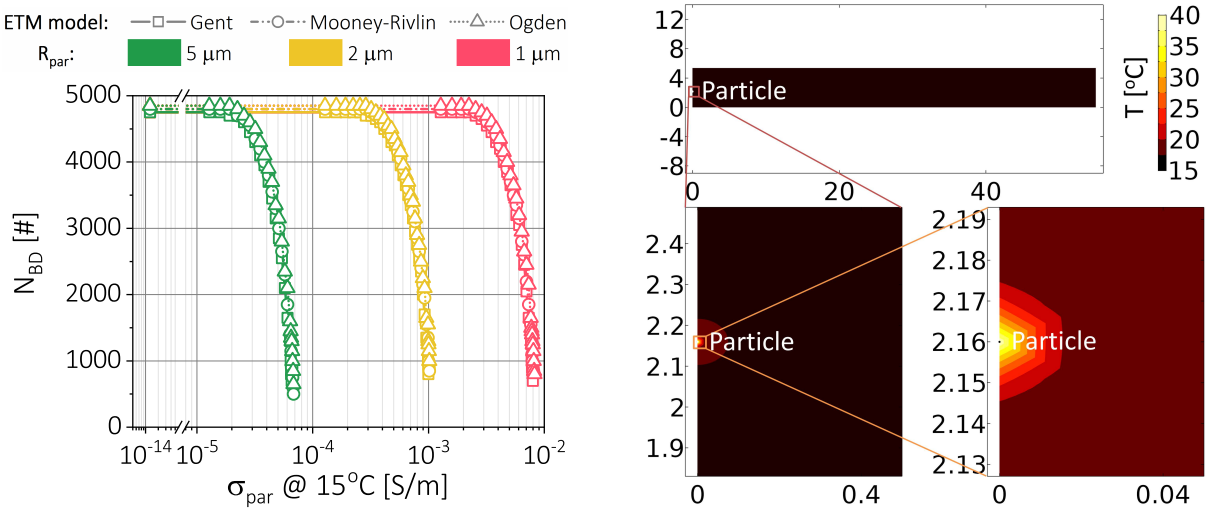

(a) N_{BD} as a function of σ_{par} @ 15°C.

(b) Simulation of the DE stack with a particle of $R_{\mathrm{par}} = 5\,\mu$m, $N = 1300$, $\sigma_{\mathrm{par}} = 6.38 \cdot 10^{-5}$ S/m and using the Gent model.

Figure 11: Parameter study examining the effect of having a single particle with high electrical conductivity, σ_{par}. The particle is placed in the hotspot of the stack and has a radius of R_{par}.

The results of N_{BD} as a function of σ_{par} for all three ETM models are similar, and all three ETM models follow the trends described above. Consistent with previous parameter studies, using the Gent model yields a slightly more restrictive estimation of N_{BD}, whereas the Ogden model yields the least restrictive estimations. However, in this parameter study regarding inclusion of a particle with high electrical conductivity, the difference between the N_{BD} values predicted by the Gent and Ogden models are in general small and in the order of 100 layers.

Discussion

The model presented in this paper combines Joule heating in a multilayered stack of DEs with the electro-mechanical deformation of the stack, in order to simulate when thermal breakdown occurs. When including a single particle with high electrical conductivity, in order to simulate an impurity in the stack, the values of N_{BD} decrease rapidly and approach an amount of possible layers similar to those seen in real-life multilayered DE applications. This illustrates the importance of taking imperfections and impurities that inevitably will appear in a multilayered stack of DEs into account.

In addition to having imperfections in the model, it would be relevant to utilise an

expression for the electrical conductivity of the elastomer material that accounts for the dependence on both temperature and electric field. Furthermore, including temperature dependence in the hyperelastic material models would yield a more realistic prediction of the mechanical behaviour of the stack.

In this work, the solutions obtained are based on steady-state simulations of the DE stack, thus at infinite time at a given set of operating conditions. However, DEs commonly operate with frequencies in the order of kHz, so a frequency study of the model would be highly relevant, as it would incorporate the build-up of heat between cycles – and thus possibly yield lower N_{BD}-values that are more realistic.

Conclusion

In this work, an electro-thermal and -mechanical model of a multilayered stack of DEs is presented, which is able to model the behaviour of a stack of DEs and determine when thermal breakdown will occur. Three different hyperelastic material models were used to model the mechanical behaviour of the elastomer material, and it was found that using the two-parameter Gent model yields the most restrictive prediction of N_{BD}, and the six-parameter Ogden model predicts the highest N_{BD} in all cases.

A parameter study of several important parameters, both geometrical and operational, was conducted, and it was established that having an inactive area generally has little impact on the breakdown point, N_{BD}, whereas having a single particle with relatively high electrical conductivity dramatically reduces the possible amount of DE layers in a stack. Furthermore, electromechanical breakdown of the stack of DEs was observed when increasing the applied voltage.

Acknowledgements

The authors gratefully acknowledge financial support from Aage and Johanne Louis-Hansens Fond.

Notations

Abbreviations:

DE	Dielectric elastomer
ET	Electro-thermal
ETM	Electro-thermal and -mechanical
FEM	Finite-element-method
PDMS	Polydimethylsiloxane

Symbols:

A	Cross-sectional area [m^2]
C_1, C_2	Parameters in W_{MR} [Pa]
d	Initial thickness of each elastomer layer [m]
E	Electric field [V/m]
E_{ave}	Average electric field [V/m]
F	Mechanical force [N/m^2]
h	Heat transfer function [W/m^2K]
h_{t}	h on top surface [W/m^2K]
h_{b}	h on bottom surface [W/m^2K]
h_0	Heat transfer coefficient [W/m^2K]
$h_{0,\mathrm{t}}$	h_0 of top surface [W/m^2K]
$h_{0,\mathrm{b}}$	h_0 of bottom surface [W/m^2K]
$h_{0,\mathrm{c}}$	h_0 of cylindrical surface [W/m^2K]
I_1	First strain invariant [-]
I_2	Second strain invariant [-]
J_{m}	Parameter in W_{G} [-]
k	Thermal conductivity [W/mK]
N	Number of layers [#]
N_{BD}	Possible number of layers before breakdown [#]
$N_{\mathrm{BD,ET}}$	N_{BD} for ET model [#]
$N_{\mathrm{BD,ETM}}$	N_{BD} for ETM model [#]
q	Generated thermal energy pr. volume [W/m^3]
r	Radial coordinate [m]
r_{HS}	r-coordinate of hotspot [m]
r_{par}	r-coordinate of entrapped particle [m]

R	Electrical resistance [Ω]
R_{A}	Radius of active part [m]
R_{I}	Radial width of inactive part [m]
R_{par}	Radius of the entrapped particle [m]
T	Temperature [K]
T_0	Ambient temperature [K]
V	Applied voltage [V]
$\mathrm{Vol{:}A_{surf}}$	Volume-to-surface-area-ratio [m]
$\mathrm{Vol_0{:}A_{0,surf}}$	$\mathrm{Vol{:}A_{surf}}$ of stack with no inactive area [m]
W	Strain energy density [Pa]
W_{G}	Gent strain energy density [Pa]
W_{MR}	Mooney-Rivlin strain energy density [Pa]
W_{O}	Ogden strain energy density [Pa]
Y	Young's modulus [Pa]
z	Axial coordinate [m]
z_{HS}	z-coordinate of hotspot [m]
z_{max}	Height of the DE stack after deformation [m]
$\alpha_1, \alpha_2, \alpha_3$	Parameters in W_{O} [-]
β_{Arr}	Parameter in $\sigma_{\mathrm{Arr}}(T)$ [K]
ϵ_r	Relative permittivity [-]
λ_i	Stretch ratio in i^{th}-direction [-]
λ_z	Stretch ratio in z-direction [-]
$\mu_1, \mu_2\, \mu_3$	Parameters in W_{O} [Pa]
σ	Electrical conductivity [S/m]
σ_{Arr}	Arrhenius expression of σ as function of temperature [S/m]
σ_{par}	σ of entrapped particle [S/m]
$\sigma_{0,\mathrm{Arr}}$	Parameter in $\sigma_{\mathrm{Arr}}(T)$ [S/m]

References

1 Pelrine RE., Kornbluh RD., Joseph JP. Electrostriction of polymer dielectrics with compliant electrodes as a means of actuation. *Sens. Actuators A Phys.* 1998;64(1):77–85.

2 Carpi F, Rossi DD, Kornbluh R, Pelrine R, Sommer-Larsen P, eds. *Dielectric elastomers as electromechanical transducers.* 1st ed. Oxford: Elsevier Ltd.; 2008

3 Biggs J, Danielmeier K, Hitzbleck J, et al. Electroactive polymers: developments of and perspectives for dielectric elastomers. *Angew. Chemie.* 2013;52(36):9409–9421.

4 Jordi C, Michel S, Fink E. Fish-like propulsion of an airship with planar membrane dielectric elastomer actuators. *Bioinspir. Biomim.* 2010;5(2):026007.

5 Kovacs G, Lochmatter P, Wissler MT. Arm wrestling robot driven by dielectric elastomer actuators. *Smart Mater. Struct.* 2007;16:S306–S317.

6 Mulgaonkar AP, Kornbluh R, Herr H. *A new frontier for orthotics and prosthetics: Application of dielectric elastomer actuators to bionics.* In: Carpi F, Rossi DD, Kornbluh R, Pelrine R, Sommer-Larsen P, eds. *Dielectric elastomers as electromechanical transducers.* 1st ed. Oxford: Elsevier Ltd.; 2008;189–206.

7 Nguyen CT, Phung H, Nguyen TD, et al. A small biomimetic quadruped robot driven by multistacked dielectric elastomer actuators. *Smart Mater. Struct.* 2014;23:065005.

8 Prahlad H, Kornbluh R, Pelrine R, Stanford S, Eckerle J, Oh S. Polymer power: Dielectric elastomers and their applications in distributed actuation and power generation. *Proc. ISSS.* Bangalore, India, 2005;100–107.

9 Wattez A, Van Kessel R. Using electro active polymers to transform wave energy conversion. *Proc. Annu. Offshore Technol. Conf.* Houston, Texas, 2016;4:2–5.

10 Brochu P, Pei Q. Advances in dielectric elastomers for actuators and artificial muscles. *Macromol. Rapid Commun.* 2010;31(1):10–36.

11 Choi HR, Kim D, Chuc NH, et al. Development of integrated tactile display devices. *Proc. SPIE.* 2009;7287(1):72871C.

12 Madsen FB, Daugaard AE, Hvilsted S, Skov AL. The current state of silicone-based dieletric elastomer transducers. *Macromol. Rapid Commun.* 2016;37(5):378–413.

13 Rosset S, Shea HR. Flexible and stretchable electrodes for dielectric elastomer actuators. *Appl. Phys. A.* 2013;110(2):281–307.

14 Kornbluh RD, Pelrine R, Prahlad H, et al. Dielectric elastomers: Stretching the capabilities of energy harvesting. *MRS Bull.* 2012;37(3):246–253.

15 Romasanta LJ, Lopez-Manchado MA, Verdejo R. Increasing the performance of dielectric elastomer actuators: A review from the materials perspective. *Prog. Polym. Sci.* 2015;51:188–211.

16 Carpi F, Salaris C, Rossi DD. Folded dielectric elastomer actuators. *Smart Mater. Struct.* 2007;16(2):S300–S305.

17 Jean P, Wattez A, Ardoise G, et al. Standing wave tube electro active polymer wave energy converter. *Proc. SPIE.* 2012;8340(1):83400C.

18 Dissado LA, Fothergill JC. *Electrical degradation and breakdown in polymers.* 1st ed. London: Peter Peregrinus Ltd.; 1992.

19 Skov AL. *Silicone-based dielectric elastomers.* Dr. Techn. Technical University of Denmark. 2016.

20 Fothergill JC, Eccles A, Houlgreave JA, Dissado LA. Water tree inception and its dependence upon electric field, voltage and frequency. *IEE Proc. A.* 1993;140(5):397–403.

21 Li K, Zhou K, Yang M, Huang M, He Y. The acceleration effect of temperature change on water tree propagation. *Proc. Int. Conf. Cond. Monit. Diagnosis.* 2016;102–105.

22 Muffoletto DP, Burke KM, Zirnheld JL. Partial discharge monitoring in dielectric elastomer actuators. *IEEE Int. Pulsed Power Conf.* 2013;6627683.

23 Huang R, Suo Z. Electromechanical phase transition in dielectric elastomers. *Proc. R. Soc. A.* 2012;468(2140):1014–1040.

24 Skov AL, Yu L. Optimization techniques for improving the performance of silicone-based dielectric elastomers. *Adv. Eng. Mater.* 2017;1700762:1–21.

25 Razak AHA, Yu L, Skov AL. Voltage-stabilised elastomers with increased relative permittivity and high electrical breakdown strength by means of phase separating binary copolymer blends of silicone elastomers. *RSC Adv.* 2017;7:17848–17856.

26 Zakaria SB, Morshuis PHF, Benslimane MY, Gernaey KV, Skov AL. The electrical breakdown of thin dielectric elastomers: thermal effects. *Proc. SPIE.* 2014;9056:90562V.

27 La TG, Lau GK. Very high dielectric strength for dielectric elastomer actuators in liquid dielectric immersion. *Appl. Phys. Lett.* 2013;102(19):192905.

28 La TG, Lau GK. Inhibiting electro-thermal breakdown of acrylic dielectric elastomer actuators by dielectric gel coating. *Appl. Phys. Lett.* 2016;108(1):12903.

29 Gatti D, Haus H, Matysek M, Frohnapfel B, Tropea C, Schlaak HF. The dielectric breakdown limit of silicone dielectric elastomer actuators. *Appl. Phys. Lett.* 2014;104(5):052905.

30 Koh SJA, Zhao X, Suo Z. Maximal energy that can be converted by a dielectric elastomer generator. *Appl. Phys. Lett.* 2009;94(26):36–38.

31 Liu LW, Zhang Z, Liu YJ, Leng JS. Failure modeling of folded dielectric elastomer actuator. *Sci. China Physics, Mech. Astron.* 2014;57(2):263–272.

32 Moscardo M, Zhao X, Suo Z, Lapusta Y. On designing dielectric elastomer actuators. *J. Appl. Phys.* 2008;104(9):1–7.

33 Qu S, Suo Z. A finite element method for dielectric elastomer transducers. *Acta Mech. Solida Sin.* 2012;25(5):459–466.

34 Yong H, He X, Zhou Y. Electromechanical instability in anisotropic dielectric elastomers. *Int. J. Eng. Sci.* 2012;50(1):144–150.

35 Zhao X, Suo Z. Method to analyze electromechanical stability of dielectric elastomers. *Appl. Phys. Lett.* 2007;91:061921.

36 Zhu J, Stoyanov H, Kofod G, Suo Z. Large deformation and electromechanical instability of a dielectric elastomer tube actuator. *J. Appl. Phys.* 2010;108(7):1–6.

37 Zurlo G, Destrade M, DeTommasi D, Puglisi G. Catastrophic thinning of dielectric elastomers. *Phys. Rev. Lett.* 2017;118:078007.

38 Christensen LR, Hassager O, Skov AL. Electro-thermal model of thermal breakdown in multilayered dielectric elastomers. *AIChE J.* 2019;65(2):859–864.

39 Bluestar Silicones. *BLUESIL RTV 141 A & B.* Url: www.benam.co.uk/skin/frontend/default/bam/ds/RTV141-TDS.pdf, Accessed 2020-01-13.

40 Clement KH, Fangel P, Jensen AD, Thomsen K. *Kemiske enhedsoperationer.* 5th ed. Lyngby, Denmark: Polyteknisk Forlag; 2009.

41 Meunier L, Chagnon G, Favier D, Orgéas L, Vacher P. Mechanical experimental characterisation and numerical modelling of an unfilled silicone rubber. *Polym. Test.* 2008;27(6):765–777.

42 Carpi F, Anderson I, Bauer S, et al. Standards for dielectric elastomer transducers. *Smart Mater. Struct.* 2015;24(10):25.

43 Horgan CO. The remarkable Gent constitutive model for hyperelastic materials. *Int. J. Non. Linear. Mech.* 2015;68:9–16.

568 44 Ogden RW, Saccomandi G, Sgura I. Fitting hyperelastic models to experimental data. *Comput. Mech.*
569 2004;34(6):484–502.

570 45 Araromi OA, Conn AT, Ling CS, Rossiter JM, Vaidyanathan R, Burgess SC. Spray deposited mul-
571 tilayered dielectric elastomer actuators. *Sens. Actuators A Phys.* 2011;167(2):459–467.

572 46 Clark RP, Presten TD, Gorden-Nesbitt DC, Malka S, Sinclair L. The size of airborne dust particles
573 precipitating broncospasm in house dust sensitive children. *J. Hyg. (Lond).* 1976;77(3):321–325.

574 47 Gaunt LF, Jerrim KL, Hughes JF. Electrostatic control of domestic dust and allergen particles for
575 improved air quality. *Powder Technol.* 2003;135-136:354–360.

576 48 Clean Air Technology. *What is a Cleanroom?* Url: www.cleanairtechnology.com/cleanroom-
577 classifications-class.php, Accessed 2020-01-13.